Dislocation structures and electrical conduction properties of low angle tilt grain boundaries in LiNbO₃

Yuho Furushima, Atsutomo Nakamura' , Eita Tochigi, Yuichi Ikuhara, Kazuaki Toyoura, and Katsuyuki Matsunaga

Articles you may be interested in

Pressure-induced phase transition of calcite and aragonite: A first principles study
Journal of Applied Physics **120**, 142118 (2016); 10.1063/1.4961723

First principles calculation of thermal expansion coefficients of pure and Cr doped α-alumina crystals
Journal of Applied Physics **120**, 142106 (2016); 10.1063/1.4961720

Single atom visibility in STEM optical depth sectioning
Applied Physics Letters **109**, 163102 (2016); 10.1063/1.4965709

First-principles analysis of X-ray magnetic circular dichroism for transition metal complex oxides
Journal of Applied Physics **120**, 142104 (2016); 10.1063/1.4961713

Dislocation structures and electrical conduction properties of low angle tilt grain boundaries in LiNbO₃

Yuho Furushima,[1] Atsutomo Nakamura,[1,a)] Eita Tochigi,[2] Yuichi Ikuhara,[2,3] Kazuaki Toyoura,[1] and Katsuyuki Matsunaga[1,3]

[1]*Department of Materials Science and Engineering, Nagoya University, Furo-cho, Chikusa-ku, Nagoya 464-8603, Japan*
[2]*Institute of Engineering Innovation, The University of Tokyo, 2-11-16, Yayoi, Bunkyo-ku, Tokyo 113-8656, Japan*
[3]*Nanostructures Research Laboratory, Japan Fine Ceramics Center, 2-4-1, Mutsuno, Atsuta-ku, Nagoya 456-8587, Japan*

Dislocations in crystalline materials constitute unique, atomic-scale, one-dimensional structure and have a potential to induce peculiar physical properties that are not found in the bulk. In this study, we fabricated LiNbO₃ bicrystals with low angle tilt grain boundaries and investigated the relationship between the atomic structure of the boundary dislocations and their electrical conduction properties. Observations by using transmission electron microscopy revealed that dislocation structures at the (0001) low angle tilt grain boundaries depend on the tilt angle of the boundaries. Specifically, the characteristic dislocation structures with a large Burgers vector were formed in the boundary with the tilt angle of 2°. It is noteworthy that only the grain boundary of 2° exhibits distinct electrical conductivity after reduction treatment, although LiNbO₃ is originally insulating. This unique electrical conductivity is suggested to be due to the characteristic dislocation structures with a large Burgers vector. *Published by AIP Publishing.* [http://dx.doi.org/10.1063/1.4961706]

I. INTRODUCTION

Dislocations in crystalline materials play an essential role not only in mechanical properties but also in functional properties. A dislocation has a dangling bond array at its core, and a localized strain field is induced in the vicinity of the core. Moreover, local nonstoichiometry can take place at the dislocation cores in ionic crystals.[1–6] As a result, the core structure of dislocations can affect various physical properties of crystals such as electrical properties,[7–10] optical properties,[11] and magnetic properties.[12] For example, dislocations in some oxide crystals are known to induce segregation of impurities and thereby exhibit peculiar electronic conductivity.[13–16] Therefore, it is significant to clarify the relationship between dislocation structures and the effect on physical properties.

To date, a great number of studies have been done by using the bicrystals with low angle tilt grain boundaries for understanding the structures and properties of boundaries and dislocations.[5,8–10,15–25] A low angle tilt grain boundary generally consists of a periodic array of edge dislocations that have a Burgers vector perpendicular to the boundary plane. Additionally, the interval of dislocations is inversely proportional to the tilt angle of the boundary according to the Frank's formula.[26] It should be noted that desirable dislocation structures can be introduced in the bicrystals with low angle tilt grain boundaries. In some multiple oxides, actually, the effects of the dislocations on electrical properties have been reported due to the systematic measurements using low

angle tilt grain boundaries with different boundary planes or with different tilt angles.[8–10] Thus, low angle grain boundaries are useful for the investigation of the structure and properties of dislocations.

Lithium niobate (LiNbO₃) is known to be a ferroelectric material used in many devices because of its linear piezoelectric response and excellent electro-optic properties. The crystal structure of LiNbO₃ in the ferroelectric phase belongs to the $R3c$ space group with lattice constants $a = 0.515$ nm and $c = 1.386$ nm,[27,28] and the spontaneous polarization exists along the [0001] direction. Additionally, it has been reported that electronic conductivity of LiNbO₃ single crystals depends on the amount of point defects.[29,30] Nakamura *et al.* observed the (11$\bar{2}$0) low angle tilt grain boundary in LiNbO₃ by using high resolution transmission electron microscopy (HRTEM).[25] They first reported that the boundary consists of 1/3[11$\bar{2}$0] basal edge dislocations, which dissociate into two partial dislocations with $b = 1/3[01\bar{1}0]$ and $b = 1/3[10\bar{1}0]$. However, there have been no reports on physical properties of the dislocations in LiNbO₃. In the case of ferroelectric materials, the structural strain along the polarization induces electric charge due to the piezoelectric effect. There is a possibility that the localized strain around a dislocation may bring about unusual phenomena in ferroelectric materials.

In this study, therefore, we investigated the atomic structures and electrical properties of dislocations in LiNbO₃ by using the bicrystals with low angle tilt grain boundaries. We fabricated three types of low angle tilt grain boundaries with different boundary planes and different tilt angles: (11$\bar{2}$0)/[1$\bar{1}$00] 1° tilt grain boundary, (0001)/[11$\bar{2}$0] 0.3° tilt grain boundary, and (0001)/[11$\bar{2}$0] 2° tilt grain boundary. The dislocations at the (11$\bar{2}$0)/[1$\bar{1}$00] boundary should have a Burgers

vector perpendicular to the polarization from geometrical considerations, while the dislocations at the $(0001)/[11\bar{2}0]$ boundaries should have a Burgers vector parallel to the polarization. Therefore, it is expected that the dislocation at the $(0001)/[11\bar{2}0]$ boundary can induce more intense strain along the polarization than dislocation at the $(11\bar{2}0)/[1\bar{1}00]$ boundary. The resulting structures of boundary dislocations were analyzed by transmission electron microscopy (TEM) and scanning TEM (STEM) in detail, and the electrical conduction properties along the dislocations were evaluated by the direct current (DC) method.

II. EXPERIMENTAL PROCEDURE

Congruent $LiNbO_3$ single-crystal plates grown by the Czochralski method[31,32] were used to fabricate bicrystals with a low angle tilt grain boundary. The size of each plate was $10 \times 10 \times 1 \, mm^3$, and their surfaces were polished by the diamond suspensions to achieve a mirror finish. These plates were joined by diffusion bonding in air at $800\,°C$ for 10 h under an additional pressure of 0.1 MPa to obtain the bicrystals with the size of $10 \times 10 \times 2 \, mm^3$. Figure 1 shows schematic illustrations of the fabricated bicrystals in this study. The bicrystals in Figs. 1(a) and 1(b) include a $(11\bar{2}0)/[1\bar{1}00]$ tilt grain boundary and a $(0001)/[11\bar{2}0]$ tilt grain boundary, respectively. Here, the crystal structure of $LiNbO_3$ has a rhombohedral symmetry. Note that the orientational relationships of the grain boundaries in Figs. 1(a) and 1(b) can be expressed as the $(0\bar{1}1)_R/[\bar{2}11]_R$ tilt grain boundary and $(111)_R/[0\bar{1}1]_R$ tilt grain boundary in the case of the rhombohedral setting, respectively.

The red lines in these figures show the dislocation lines induced at the boundaries. The tilt angle 2θ at the $(11\bar{2}0)/[1\bar{1}00]$ tilt grain boundary was set to be $1°$. Meanwhile, in the case of the $(0001)/[11\bar{2}0]$ tilt grain boundary, two different tilt angles were chosen for $0.3°$ and $2°$. Here, polarizations of these single-crystal plates were set to be the same direction. The temperature of $800\,°C$ (1073 K) for bonding is sufficiently lower than the Curie point of $\sim 1140\,°C$ ($\sim 1413\,K$).[33] It is thus expected that the polarization in crystals is preserved during the bonding process. After the bicrystals were fabricated, several slices with the size of about $2 \times 0.3 \times 2 \, mm^3$ were cut out from them for TEM observations and electrical measurements.

Slices of the bicrystals were mechanically ground to a thickness of about $50\,\mu m$ and attached with a stainless-steel single hole mesh for reinforcement. The center of the sample including a grain boundary was milled by the Ar^+ ion beam to obtain electron transparency. The samples were observed using a conventional TEM (JEOL JEM-2010HC, 200 kV) and a scanning TEM (STEM: JEOL JEM-ARM200F, 200 kV). For STEM observations, we employed the high angle annular dark field (HAADF) method using a 90–370 mrad detector.

The electrical properties along the boundaries were measured by the DC method. Specimens cut out from the fabricated bicrystals were annealed at $500\,°C$ for 10 h in a reducing atmosphere of Ar-$4\%H_2$ to increase carriers for electrical conduction, and they were mechanically polished by diamond suspensions to remove the surface layer. Then, tungsten electrodes were sputtered on opposite faces of the specimens. Figure 2 shows a micrograph of a prepared specimen and schematic illustration of the measurement. The current-voltage (I-V) characteristics along the boundary dislocations were investigated by dc voltage from -20 to 20 V at room temperature, and temperature dependence of electrical conductivity was investigated in the 20–100 °C temperature range.

III. RESULTS AND DISCUSSION

Figure 3 shows a typical bright field TEM image of the $(11\bar{2}0)/[1\bar{1}00]$ 1° tilt grain boundary and the corresponding selected-area diffraction pattern. It was confirmed that the
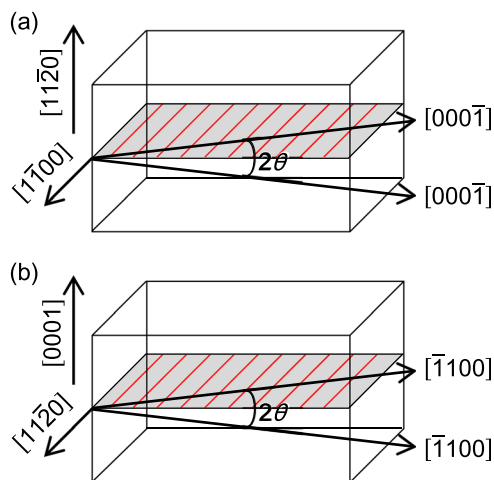

FIG. 1. Schematic illustration showing crystallographic orientations of fabricated bicrystals in this study. (a) Bicrystal with a $(11\bar{2}0)/[1\bar{1}00]$ low angle tilt grain boundary. The tilt angle 2θ was set to be $1°$. (b) Bicrystal with a $(0001)/[11\bar{2}0]$ low angle tilt grain boundary. The tilt angle 2θ was set to be $0.3°$ and $2°$.
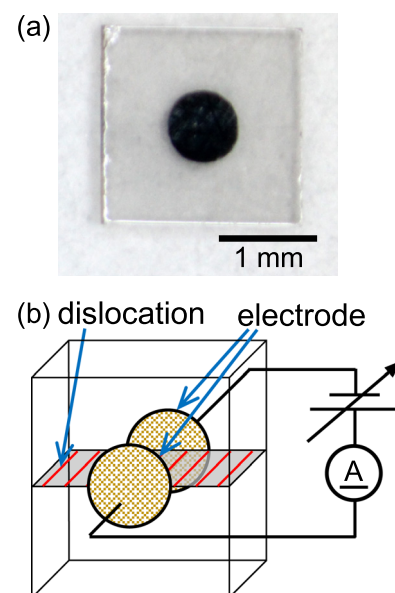

FIG. 2. (a) A micrograph of a typical specimen prepared for the electrical measurement. Tungsten electrodes were sputtered on the top and bottom surfaces of the specimen. (b) Schematic illustration of the electrical measurement performed in this study.
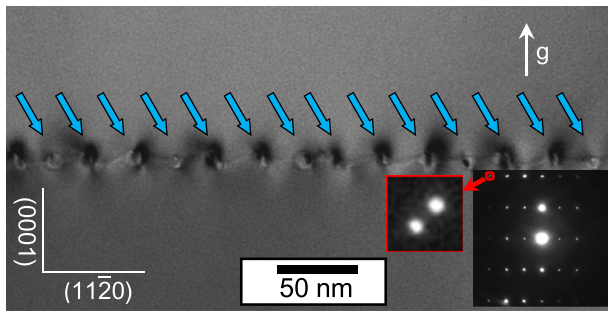
FIG. 3. A typical bright field TEM image obtained at the $(11\bar{2}0)/[1\bar{1}00]$ 1° tilt grain boundary. Contrasts due to dislocations are arranged along the boundary. The selected-area diffraction pattern taken from this area is the inset at the bottom right, and the part enclosed by the red line indicates the magnified diffraction spots.

single-crystal plates were bonded successfully, and the periodic contrasts appeared at the boundary (indicated by blue arrows in the figure) were considered to be due to the introduced boundary dislocations. As can be seen from the diffraction pattern, the diffraction spots from the two grains are well separated from each other. The angle between these two spots is estimated to be approximately 1° which corresponds to the designed tilt angle. The interval between two neighbor contrasts is about 25 nm. Here, the interval of the boundary dislocations d can be simply found from the tilt angle 2θ according to the Frank's formula:[26] $d = b/2\theta$, where b is the magnitude of the component perpendicular to the boundary plane of the Burgers vector of dislocations. When $2\theta = 1.0°$ and $b = 0.515$ nm are applied to this formula for the $1/3[11\bar{2}0]$ vector that is the minimum translation vector perpendicular to the $(11\bar{2}0)$ boundary plane, the interval is calculated to be 29 nm. This interval is approximately in agreement with the
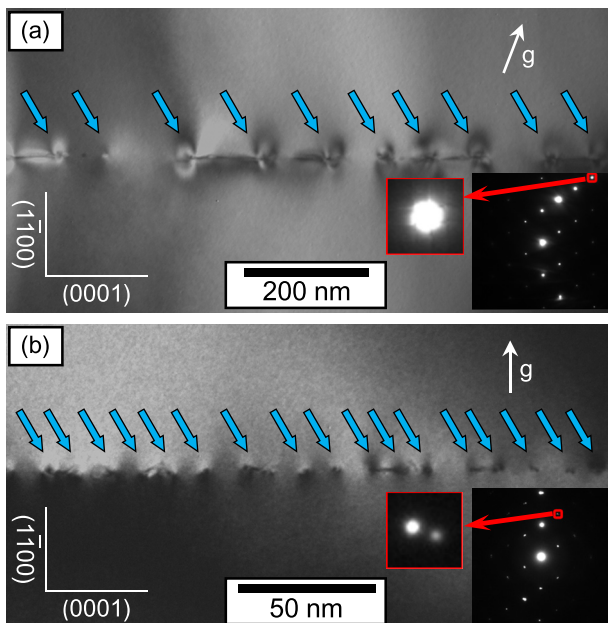
observed one of 25 nm. Meanwhile, Figs. 4(a) and 4(b) show typical TEM images of the $(0001)/[11\bar{2}0]$ tilt grain boundaries with the tilt angles of 0.3° and 2°, respectively. It was also confirmed from the diffraction patterns that the 2° tilt grain boundary was formed as designed. In contrast, the diffraction spots in the boundary of 0.3° were not separated in spite of the misorientation. This is believed to be due to the too low misorientation angle. The contrasts indicated by blue arrows in Fig. 4 are believed to be due to the introduced boundary dislocations, and the intervals of the contrasts were roughly estimated to be 97 nm for the 0.3° boundary and 13 nm for the 2° boundary. If the boundaries consist of the dislocations with $b = [0001]$, which is the minimum translation vector perpendicular to the (0001) boundary plane, the intervals are calculated to be 265 nm for the 0.3° boundary and 40 nm for the 2° boundary according to the Frank's formula. However, it is apparent that the calculated intervals are about three times wider than the observed ones. This implies that the $(0001)/[11\bar{2}0]$ tilt grain boundaries consist of the dislocations with a Burgers vector smaller than $b = [0001]$.

Figure 5(a) shows a typical HAADF-STEM image of a dislocation at the $(11\bar{2}0)/[1\bar{1}00]$ tilt grain boundary taken along the $[1\bar{1}00]$ direction, and Fig. 5(b) represents a schematic illustration of the $[1\bar{1}00]$ view of the LiNbO$_3$ crystal
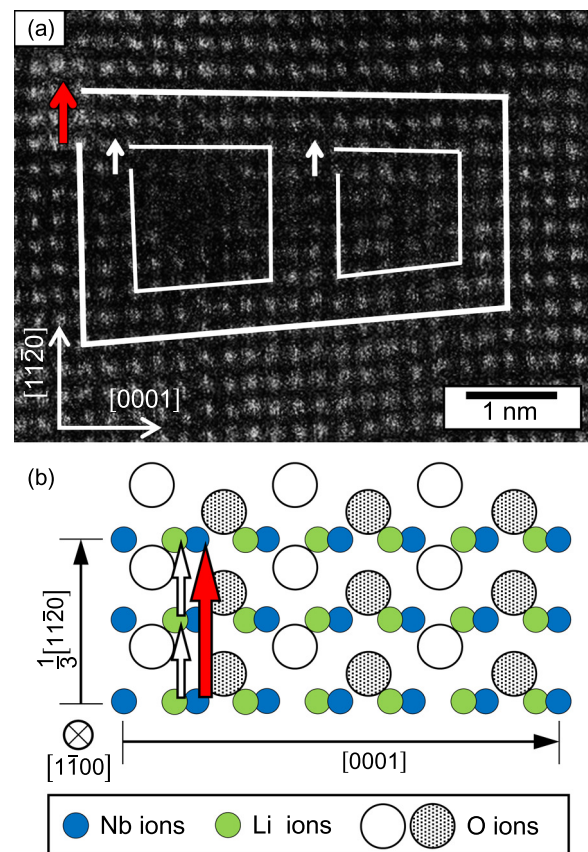

FIG. 5. (a) HAADF-STEM image including partial dislocation pairs observed at the $(11\bar{2}0)/[1\bar{1}00]$ 1° tilt grain boundary from the $[1\bar{1}00]$ view. The Burgers circuits indicate that the partial dislocation pair has the $1/3[11\bar{2}0]$ edge component in total. (b) Schematic illustration showing the crystal structure of LiNbO$_3$ projected along the $[1\bar{1}00]$ direction. The red and open arrows indicate the Burgers vectors of the perfect and partial dislocations, respectively.

FIG. 4. Typical bright field images of the $(0001)/[11\bar{2}0]$ tilt grain boundaries. The boundary in (a) has a tilt angle of 0.3°, while that in (b) has a tilt angle of 2°. The blue arrows indicate the contrasts which are considered to be due to dislocations. The selected-area diffraction patterns taken from these areas are the inset at the bottom right, and the parts enclosed by the red line are magnified diffraction spots.

structure. The bright spots in the HAADF-STEM image correspond to the positions of Nb atom columns because the Nb atom has the largest atomic number of constituent atoms of $LiNbO_3$. It was found that pairs of lattice discontinuities with the very narrow separation distance of 2–3 nm are arranged at the $(11\bar{2}0)/[1\bar{1}00]$ tilt grain boundary. As can be seen from the Burgers circuits in Fig. 5(a), each partial dislocation has a lattice discontinuity of $1/6[11\bar{2}0]$ in the $(1\bar{1}00)$ projection, and the total edge component of the partial dislocation pair is $1/3[11\bar{2}0]$. This means that the boundary dislocations with $\boldsymbol{b} = 1/3[11\bar{2}0]$ dissociate into two partial dislocations. In this case, a stacking fault is formed along the $(11\bar{2}0)$ plane between the two partials. Nakamura *et al.* reported on the basis of HRTEM observation that the $1/3[11\bar{2}0]$ dislocations at the $(11\bar{2}0)/[1\bar{1}00]$ tilt grain boundary dissociate into two partial dislocations according to the following equation:[25]

$$1/3[11\bar{2}0] = 1/3[01\bar{1}0] + 1/3[10\bar{1}0].$$

This dissociation reaction is also indicated by the arrows in Fig. 5(b). The red arrow corresponds to $1/3[11\bar{2}0]$, and the two open arrows correspond to $1/3[01\bar{1}0]$ and $1/3[10\bar{1}0]$. The partial dislocation with $\boldsymbol{b} = 1/3[01\bar{1}0]$ or $\boldsymbol{b} = 1/3[10\bar{1}0]$ has an edge component of $1/6[11\bar{2}0]$ in the $[1\bar{1}00]$ view, which coincides with the dislocation structure observed in the present study. Therefore, the $(11\bar{2}0)/[1\bar{1}00]$ 1° tilt grain boundary consists of the dislocations of $\boldsymbol{b} = 1/3[11\bar{2}0]$ as

reported in the former paper. In contrast, Ohno *et al.*[34] recently reported that the $1/3[11\bar{2}0]$ basal dislocations did not seem to dissociate into partials according to their experimental results using conventional TEM. In general, it is difficult for usual conventional TEM to analyze small structures due to the limited resolution. The discrepancy between the two reports may be due to the too narrow separation distance between the partials.

In the $(0001)/[11\bar{2}0]$ 0.3° and 2° tilt grain boundaries, two types of dislocation structures were typically observed. Figure 6 shows HAADF-STEM images of the two types of dislocations, and their filtered inverse fast-Fourier-transferred (FFT) images for the same areas. The vertical and horizontal fringes in the inverse FFT images correspond to the (0006) and $(6\bar{6}00)$ planes, respectively. It was found that the two kinds of dislocations with the different Burgers vectors are primarily formed along the boundaries, which are separately shown in (a) and (b). The dislocation on the HAADF-STEM image in (a) totally has an edge component of $1/3[\bar{1}101]$, which is a translation vector in the crystal structure of $LiNbO_3$. Accordingly, the dislocation in (a) is an edge dislocation with $\boldsymbol{b} = 1/3[\bar{1}101]$. On the other hand, the dislocation on the HAADF-STEM image in (b) totally has a $1/6[1\bar{1}02]$ edge component, which is not a translation vector of $LiNbO_3$. This implies that this dislocation has some screw component, because the Burgers vector of a perfect dislocation must coincide with a translation vector in the lattice. Here, the edge
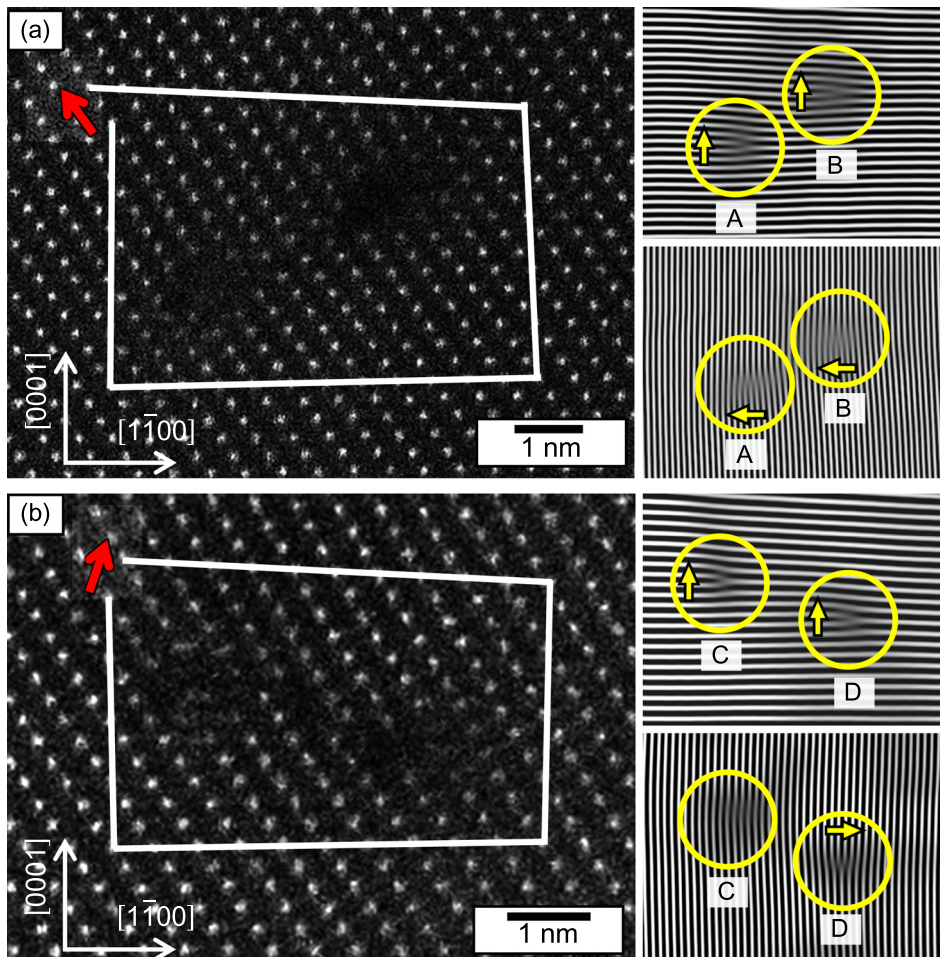

FIG. 6. HAADF-STEM images including the dislocation structures observed at the $(0001)/[11\bar{2}0]$ 2° tilt grain boundary along the $[11\bar{2}0]$ direction. Both the $(0001)/[11\bar{2}0]$ 0.3° and 2° tilt grain boundaries typically consist of these two types of dislocations. The dislocation in (a) has the edge component of $1/3[\bar{1}101]$ and that in (b) has the $1/6[1\bar{1}02]$ edge component. The figures on the right side show the inverse FFT images for the same areas. The vertical and horizontal lines correspond to the stacking of the (0006) and $(6\bar{6}00)$ planes, and the circles show the each region with the lattice discontinuity.

components of the $1/3[\bar{1}101]$ and $1/6[1\bar{1}02]$ can be further decomposed into the components perpendicular and parallel to the boundary: $1/3[\bar{1}101] = 1/3[0001] + 1/3[\bar{1}100]$, $1/6[1\bar{1}02] = 1/3[0001] + 1/6[1\bar{1}00]$. It can be seen that both the two dislocations have the component of $1/3[0001]$, which contributes to compensating the given tilt angle at the boundary.

Two lattice discontinuities are clearly present with a separation distance of a few nanometers in the inverse FFT images in Fig. 6. This means that the boundary dislocations dissociate into two partial dislocations. As for the dislocation dissociation in Fig. 6(a), each partial dislocation marked with A and B was found to have the same edge component of $1/6[\bar{1}101]$, which is divided into the two lattice discontinuities of $1/6[0001]$ and $1/6[\bar{1}100]$ as can be seen from the individual inverse FFT images. Meanwhile, in the case of the partial dislocations marked with C and D in Fig. 6(b), the two partial dislocations have different edge components. That is, the partial dislocation C has only the lattice discontinuity of $1/6[0001]$ although the partial dislocation D totally has a lattice discontinuity of $1/6[\bar{1}101]$. Here, note the configuration of the two partial dislocations. A stacking fault is formed between the partial dislocations due to dislocation dissociation. It can be seen that the two partial dislocations in Figs. 6(a) and 6(b) are not present on the (0001) plane. Namely, the stacking fault plane between the two partials is deviated from the (0001) boundary plane. This configuration is special because boundary dislocations ordinarily dissociate into partials along the boundary plane.[18–25] It is known that the dislocations with the edge component tend to arrange linearly to decrease the static elastic energy around dislocations according to the Peach-Koehler formula.[35] Note that the partial dislocations marked with A and B in Fig. 6(a) have the same edge components of $1/6[\bar{1}101]$. In this case, a force acts so that the extra half plane that originated from their edge components arrange on the same plane. This force is probably the reason why the configuration of the two partials is not along the boundary plane. As for the partial dislocation pair in Fig. 6(b), likewise, the partial dislocation D has the Burgers vector inclined from [0001], resulting in the deviation of positions of the partial dislocations from the (0001) boundary plane.

Here, we will discuss about the reason why the boundary dislocations are formed as shown in Figs. 6(a) and 6(b). Figure 7 shows the crystal structure of $LiNbO_3$ and the three minimum translation vectors with a component along the [0001] direction: $1/3[\bar{1}101]$, $1/3[0\bar{1}11]$, and $1/3[10\bar{1}1]$. The three vectors are indicated by the red arrows with (i), (ii), and (iii) in the figure. Note that the three are also expressed as $[100]_R$, $[010]_R$, and $[001]_R$ in the rhombohedral setting, and they are equivalent vectors from the crystallographic point of view. The Burgers vector of the dislocation in Fig. 6(a) coincides with the $1/3[\bar{1}101]$ vector marked with (i). On the other hand, the edge component of the dislocation in Fig. 6(b) of $1/6[1\bar{1}02]$ corresponds to the $(11\bar{2}0)$ projection of the $1/3[0\bar{1}11]$ or $1/3[10\bar{1}1]$ vectors, which are marked with (ii) and (iii), respectively. This suggests that the dislocation in Fig. 6(b) has a Burgers vector of either $1/3[0\bar{1}11]$ or $1/3[10\bar{1}1]$. Now the three equivalent vectors of $1/3[\bar{1}101]$, $1/3[0\bar{1}11]$, and $1/3[10\bar{1}1]$ include a component parallel to
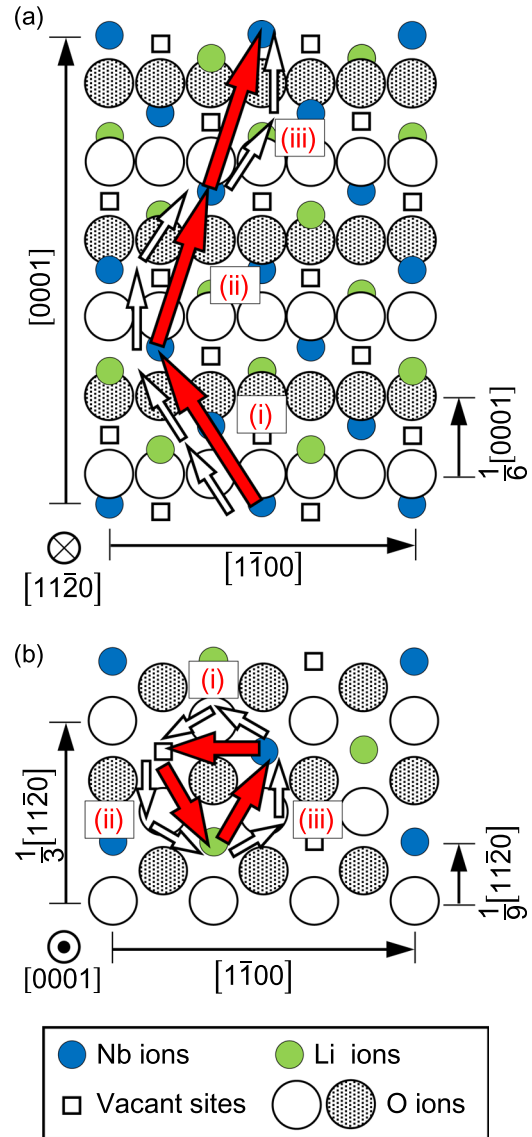

FIG. 7. Schematic illustration showing the Burgers vectors of the boundary dislocations formed at the $(0001)/[11\bar{2}0]$ tilt grain boundary. The red arrows marked with (i), (ii), and (iii) correspond to the Burgers vectors of $1/3[\bar{1}101]$, $1/3[10\bar{1}1]$, and $1/3[0\bar{1}11]$, respectively. The small open arrows show the Burgers vectors of partial dislocations by expected dissociation reaction.

the (0001) plane: $1/3[\bar{1}100]$, $1/3[0\bar{1}10]$, and $1/3[10\bar{1}0]$, respectively. These components are not needed geometrically to compensate the given tilt angles at the boundary. In order to cancel out the unnecessary components, the three $1/3\langle\bar{1}101\rangle$ dislocations should be formed in the same number at the boundary. Namely, it is apparent that the sum of the $1/3[\bar{1}101]$, $1/3[0\bar{1}11]$, and $1/3[10\bar{1}1]$ is [0001], which corresponds to a translation vector perpendicular to the boundary plane. This consideration agrees with that only two types of dislocation structures were observed by HAADF-STEM (Figs. 6(a) and 6(b)) because the $1/3[0\bar{1}11]$ and $1/3[10\bar{1}1]$ dislocations look the same in the $(11\bar{2}0)$ projection. From these things, it is suggested that the boundary consists of the three equivalent dislocations with $\boldsymbol{b} = 1/3[\bar{1}101]$, $1/3[0\bar{1}11]$, and $1/3[10\bar{1}1]$, and the triplet of the $1/3\langle\bar{1}101\rangle$ dislocations should be the basic unit to compensate the tilt angle at the

(0001)/[11$\bar{2}$0] low angle tilt grain boundaries. In this case, the ideal intervals of the dislocations are calculated to be 88 nm for the 0.3° boundary and 13 nm for the 2° boundary, which agree with the observed intervals (97 nm for the 0.3° boundary and 13 nm for the 2° boundary). It should be mentioned that the same type of dislocations with $b = 1/3 \langle \bar{1}101 \rangle$ are also formed at low-angle tilt grain boundaries in alumina (α-Al$_2$O$_3$)[24] and Bi$_2$Te$_3$.[2]

Subsequently, we consider the dissociation structures of the boundary dislocations from the observed edge components of the partial dislocations in Fig. 6. In the case of alumina with the $R\bar{3}c$ crystal structure that is similar to the $R3c$ structure of LiNbO$_3$, it has been known that the $1/3 \langle \bar{1}101 \rangle$ dislocations can dissociate as follows:[24]

(total)   (partial 1)   (partial 2)
$1/3[\bar{1}101] = 1/18[\bar{2}4\bar{2}3] + 1/18[\bar{4}223]$ (marked with (i) in Fig. 7)
$1/3[0\bar{1}11] = 1/18[\bar{2}\bar{2}43] + 1/18[2\bar{4}23]$ (marked with (ii) in Fig. 7)
$1/3[10\bar{1}1] = 1/18[4\bar{2}\bar{2}3] + 1/18[22\bar{4}3]$ (marked with (iii) in Fig. 7).

Here, the Burgers vectors of these $1/18 \langle 22\bar{4}3 \rangle$ (equivalently, $1/6 \langle 1\bar{1}3 \rangle_R$ in the rhombohedral setting) partial dislocations are indicated by the small open arrows in Fig. 7. The $1/18 \langle 22\bar{4}3 \rangle$ vectors consist of the $1/9 \langle 11\bar{2}0 \rangle$ component on (0001) and the $1/6[0001]$ component along [0001]. The (11$\bar{2}$0) projections of $1/18[\bar{2}4\bar{2}3]$, $1/18[\bar{4}223]$, $1/18[\bar{2}\bar{2}43]$, $1/18[2\bar{4}23]$, $1/18[4\bar{2}\bar{2}3]$, and $1/18[22\bar{4}3]$ vectors correspond to $1/6[\bar{1}101]$, $1/6[\bar{1}101]$, $1/6[0001]$, $1/6[1\bar{1}01]$, $1/6[1\bar{1}01]$, and $1/6[0001]$ vectors, respectively. These vectors are consistent with the edge components of the partial dislocations observed in Fig. 6. Therefore, it is reasonable to consider that $1/3 \langle \bar{1}101 \rangle$ dislocations in LiNbO$_3$ dissociate into two partial dislocations with $b = 1/18 \langle 22\bar{4}3 \rangle$ similarly to alumina. In contrast, this dissociation structure is different from the reported structure of the $1/3 \langle \bar{1}101 \rangle$ dislocations in Bi$_2$Te$_3$ with the $R\bar{3}m$ crystal structure.[2]

We should mention that characteristic dislocation structures were formed in places only at the (0001)/[11$\bar{2}$0] 2° tilt grain boundary. Figures 8(a)–8(c) show a HAADF-STEM image containing a characteristic dislocation structure and its inverse FFT images. The structure consists of four lattice discontinuities (marked with E, F, G, and H in the inverse FFT images), whose edge components correspond to $1/6[0001]$, $1/6[0001]$, $1/6[1\bar{1}01]$, and $1/6[1\bar{1}01]$, respectively, and has a $1/3[1\bar{1}02]$ edge component in total. The open arrows in Fig. 8(d) indicate the edge component of the each discontinuity, and the red arrow in the figure indicates the total edge component. The total edge component of $1/3[1\bar{1}02]$ (equivalently, $[011]_R$ in the rhombohedral setting) is a translation vector of LiNbO$_3$ and is equivalent to the sum of the two translation vectors of $1/3[0\bar{1}11]$ and $1/3[10\bar{1}1]$. As can be seen from the configuration, the left two are slightly separated from the right two although all the distances between the partials are not long. Assuming that the four partial dislocations can be divided into two pairs of right and left, therefore, the left pair of the two partial dislocations (marked with E and F) has a $1/3[0001]$ edge component, and the right pair (marked with G and H) has a $1/3[1\bar{1}01]$ edge component. The Burgers vectors having these edge components do not
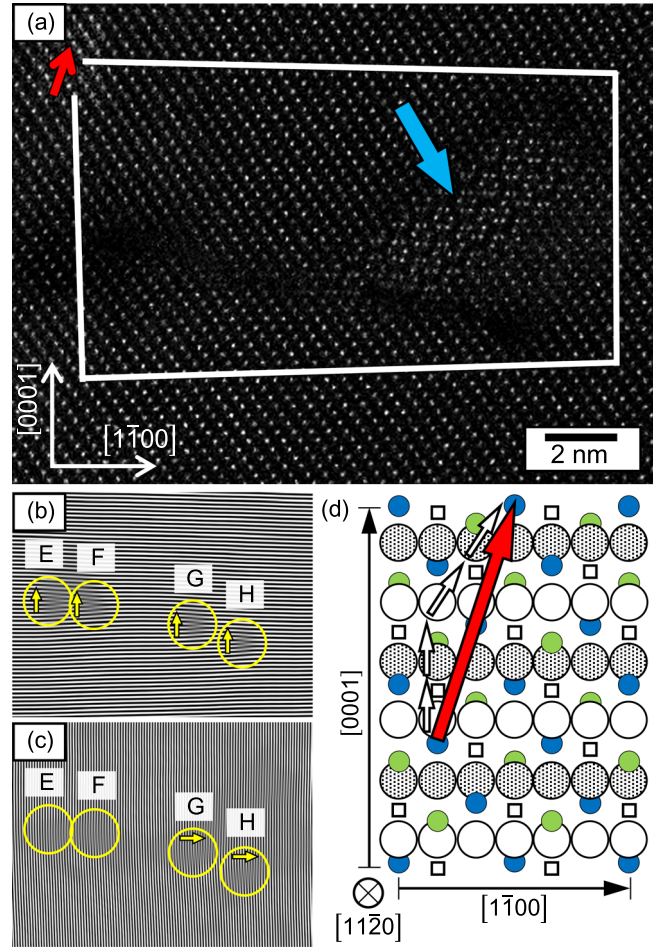

FIG. 8. (a) HAADF-STEM image of the characteristic dislocation structure observed at the (0001)/[11$\bar{2}$0] 2° tilt grain boundary. The blue arrow shows a secondary phase. (b) and (c) The inverse FFT images for the same area. (d) Schematic illustration of the Burgers vector of the characteristic dislocation structure. The small open arrows show the Burgers vectors of each partial dislocation, and the red arrow corresponds to the total discontinuity of $1/3[1\bar{1}02]$.

coincide with any of the translation vectors in LiNbO$_3$ even if any screw components are added. Additionally, the separation distance between the partial dislocations marked with F and G is 6.1 nm, which is much narrower than the observed interval of the perfect dislocations (13 nm). Therefore, it can be concluded that the four partial dislocations are not from the two perfect dislocations. Namely, the dislocation structure in Fig. 8 is considered to correspond to a dislocation with $b = 1/3[1\bar{1}02]$ that dissociates into four partial dislocations with stacking faults in between. Here, presupposing that the partial dislocations have a Burgers vector of $1/18 \langle 22\bar{4}3 \rangle$ similarly to the dissociation structure of the $1/3 \langle \bar{1}101 \rangle$ dislocation, the dissociation reaction is expected as follows:

(total)   (partial 1)   (partial 2)   (partial 3)   (partial 4)
$1/3[1\bar{1}02] = 1/18[2\bar{2}43] + 1/18[22\bar{4}3] + 1/18[4\bar{2}\bar{2}3] + 1/18[2\bar{4}23]$.

It is noteworthy that this characteristic dislocation structure was not observed at the (0001)/[11$\bar{2}$0] 0.3° tilt grain boundary. This suggests that the formation of the characteristic dislocation structure with the large Burgers vector will be due

to the narrower interval of the geometrically formed dislocations at the 2° boundary. The strong interaction among the dislocations should induce such unique dislocation structure. In this case, the tilt angle at the boundary can be compensated by the pair of dislocations with $b=1/3[\bar{1}101]$ and $1/3[1\bar{1}02]$, in addition to by the triplet of the dislocations with $b=1/3[\bar{1}101]$, $1/3[0\bar{1}11]$, and $1/3[10\bar{1}1]$.

As shown in Fig. 8, in the region indicated by the blue arrow, the characteristic arrangement of the bright spots is observed, indicating a secondary phase formation. This secondary phase was frequently formed accompanied with the dislocation with $b=1/3[1\bar{1}02]$. We found that the characteristic arrangement of the bright spots agrees well with the positions of Nb atoms in $LiNb_3O_8$. Figure 9(a) shows a simulated HAADF image of the $LiNb_3O_8$ crystal structure projected from the [010] direction, in which the experimental image of the secondary phase is inserted (a region surrounded by the red line in the figure). The image simulation was obtained using the WinHREM program (HREM Research, Inc.) that is based on the multislice method.[36] Figure 9(b) shows the schematic illustration of the crystal structure of $LiNb_3O_8$. In $LiNb_3O_8$, oxygen ions are arranged approximately in hexagonal close packing similarly in $LiNbO_3$, and cations occupy 1/2 of the octahedral sites of oxygen ions. As seen in the two regions within the green boxes in Fig. 9(a), the arrangement of Nb atoms in the simulated and experimental images coincides well with each other. Therefore, it is concluded that the secondary phase is brought about by $LiNb_3O_8$. In general, the $LiNb_3O_8$ phase tends to be formed in $LiNbO_3$ due to large Li deficiency.[37,38] Additionally, dislocations are known to act as a rapid path for element diffusion in crystals due to intense strain field at and around dislocations.[39–41] The characteristic dislocation structure has a larger strain field because the Burgers vector is larger than those of the dislocations in Figs. 6(a) and 6(b) of $1/3\langle\bar{1}101\rangle$. Therefore, it is likely that the dislocation with
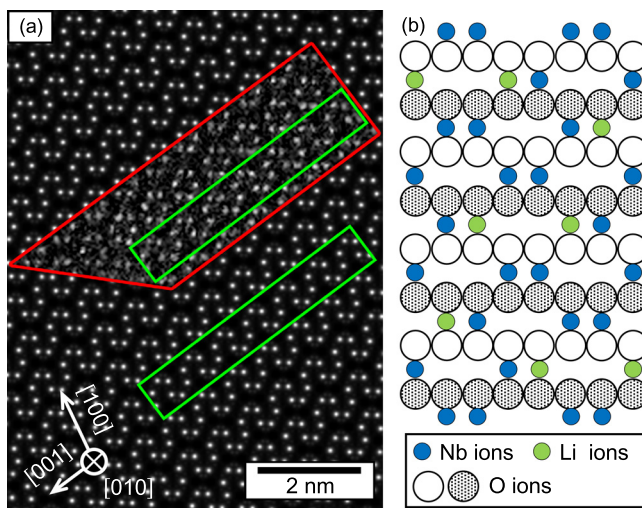
the large Burgers vector can play a role of diffusion path of the Li atoms and thereby the $LiNb_3O_8$ phase was formed at the dislocation. Such deviation of the atomic composition at dislocations has also been reported in other materials, such as Bi_2Te_3[2] and $SrTiO_3$.[3–5]

Electrical conduction properties along the boundary dislocations will be shown in this section. The I–V characteristics were investigated by applying sweep voltage to the specimens at room temperature. Figure 10 shows I–V characteristics of the regions including the boundary (boundary region) and the regions not including the boundary (bulk region) in the bicrystal specimens after the reducing treatment. Note that the specimens did not exhibit measurable electrical conductivity before reduction. It was found out that only the region including the $(0001)/[11\bar{2}0]$ 2° tilt grain boundary exhibits high electrical conductivity after the reducing treatment. In addition, the I–V characteristic was linear, which means that the contact parts between a specimen and electrodes preserve good condition. Here, remind
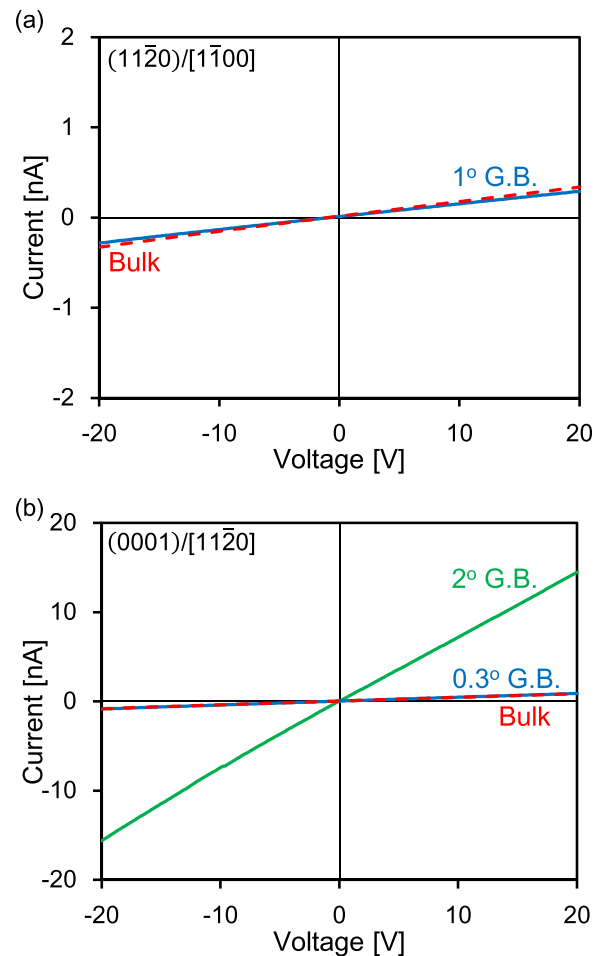
(a)

(b)

FIG. 10. (a) I–V characteristics obtained from the bicrystal with the $(11\bar{2}0)/[1\bar{1}00]$ 1° tilt grain boundary. The red dotted line and the blue line indicate the characteristics of the bulk region and the boundary region, respectively. (b) I–V characteristics obtained from the bicrystals with the $(0001)/[11\bar{2}0]$ tilt grain boundary. The green line indicates the characteristic of the boundary region with a tilt angle of 2°. The red dotted line and the blue line indicate the characteristics of the bulk region and the boundary region with a tilt angle of 0.3°, although they are almost the same. Note that the ranges of vertical axis are different for two panels.

FIG. 9. (a) Simulated HAADF-STEM image of $LiNb_3O_8$ from the [010] view. The part encircled by red line shows the secondary phase experimentally observed at the $(0001)/[11\bar{2}0]$ 2° tilt grain boundary. It can be seen that the zigzag spot patterns within the green boxes in the simulated image and in the observed image coincide with each other. (b) Schematic illustration of the $LiNb_3O_8$ crystal structure from the [010] view.

that the characteristic dislocation structures with the large Burgers vector and the $LiNb_3O_8$ phase were formed only at the $(0001)/[11\bar{2}0]$ $2°$ tilt grain boundary. Therefore, this distinct electrical conductivity will be due to the characteristic dislocation structures. To estimate the activation energy of the conduction, temperature dependence of the conductivity was investigated in the $20–100\,°C$ temperature range. Figure 11 shows the Arrhenius plot of the electrical conductivities measured in the boundary and bulk regions in the bicrystal with the $(0001)/[11\bar{2}0]$ $2°$ tilt grain boundary. According to the Arrhenius equation, the electrical conductivity is described as $\sigma = \sigma_0 \exp(-E_a/kT)$, where σ is the conductivity, σ_0 is the preexponential factor, E_a is the activation energy, k is the Boltzmann constant, and T is the temperature. By fitting the conductivity data with the Arrhenius equation, the activation energies were obtained: $0.55\,eV$ in the boundary region and $0.73\,eV$ in the bulk region.

The mechanism of charge transport in reduced $LiNbO_3$ has been suggested to be due to electron hopping.[29,30] When $LiNbO_3$ is reduced, oxygen vacancies are introduced into a crystal, and the electrons released from the neutral oxygen vacancy sites are trapped at the Nb^{5+} ions, transforming them into Nb^{4+} ions. The hopping of these electrons between Nb^{5+} and Nb^{4+} causes the electrical conduction. In the case of the electrical conduction at the $(0001)/[11\bar{2}0]$ $2°$ tilt grain boundary, the carrier is presumed to be electrons because they are induced by reducing treatment as well. However, the grain boundary has the lower activation energy than the bulk region. It is thus believed that the characteristic dislocation structures with the larger Burgers vector at the $(0001)/[11\bar{2}0]$ $2°$ tilt grain boundary provide a low energy conduction path of electrons. Here, consider the local electrical conductivity around the characteristic dislocation structures by assuming that the each conduction path is cylindrical around the characteristic dislocation structure. Figure 12 shows the local electrical conductivity estimated from the difference of the conductivity between the boundary region and bulk region at room temperature. The horizontal axis in the figure represents the postulated diameter of the cylindrical conduction path. In this calculation, we adopted a condition that the interval between the characteristic dislocations is $40\,nm$, which presupposes that the $(0001)/[11\bar{2}0]$ $2°$ tilt grain
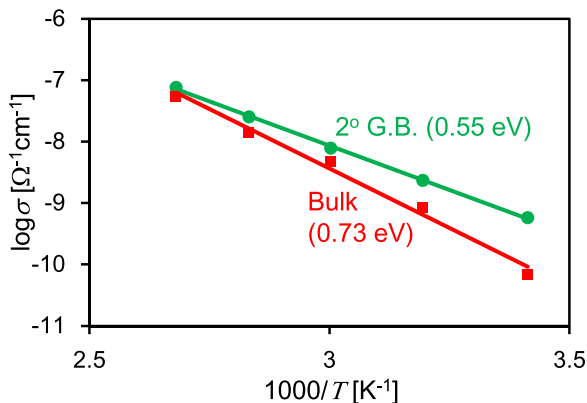

FIG. 11. Temperature dependence of the electrical conductivities in the bulk region and the boundary region including the $(0001)/[11\bar{2}0]$ $2°$ tilt grain boundary. The numbers in the parentheses represent the activation energies.
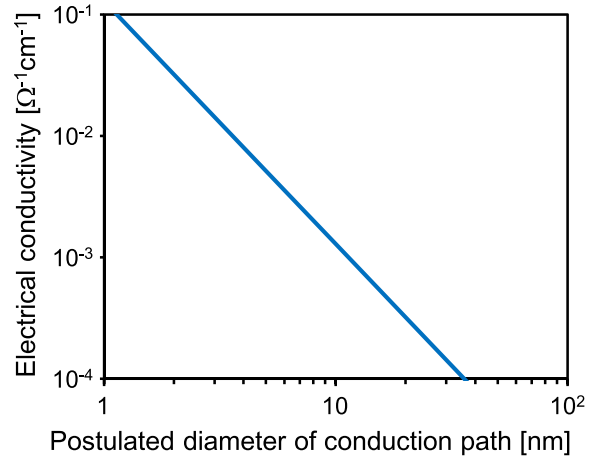

FIG. 12. Presumption of the local electrical conductivity at the $(0001)/$ $[11\bar{2}0]$ $2°$ tilt grain boundary. It was assumed that the high electrical conduction occurred around the characteristic dislocation structure, whose diameter is shown in the horizontal axis.

boundary consisted of the pairs of the characteristic dislocation with $b = 1/3[1\bar{1}02]$ and the ordinal dislocation with $b = 1/3[\bar{1}101]$. Then, the local electrical conductivity of the characteristic dislocation structure can be estimated to be $10^{-4}–10^{-3}$ $[\Omega^{-1}cm^{-1}]$ although it varies with the postulated diameter. The previous investigations reported that the electrical conductivity of reduced $LiNbO_3$ single crystals is in the range of $10^{-14}–10^{-7}$ $[\Omega^{-1}cm^{-1}]$ at room temperature depending on the reduced condition.[29,30] In addition, the electrical conductivity of $LiNb_3O_8$ was found to be much lower than the estimated local conductivity, as shown in the Appendix. It is apparent that the characteristic dislocation structure has distinctly high electrical conductivity. Therefore, the electrical conduction at the $(0001)/[11\bar{2}0]$ $2°$ tilt grain boundary cannot be explained by ordinal charge transportation in bulk $LiNbO_3$ and bulk $LiNb_3O_8$. Here, note that the Burgers vector of the characteristic dislocation at the $(0001)/[11\bar{2}0]$ $2°$ tilt grain boundary has a large edge component along the $[0001]$ direction which corresponds to the polarization direction as shown in Fig. 8. In this point, intense strain along the polarization will be induced around the characteristic dislocation. Thus, it is likely that the interaction between the polarization and lattice distortion around the characteristic dislocation with the large Burgers vector should bring about the distinct electrical conduction.

IV. CONCLUSION

Low angle tilt grain boundaries are useful to investigate the structure and properties of dislocations. In this study, three kinds of $LiNbO_3$ bicrystals with the $(11\bar{2}0)/[1\bar{1}00]$ $1°$ tilt grain boundary, $(0001)/[11\bar{2}0]$ $0.3°$ tilt grain boundary, and $(0001)/[11\bar{2}0]$ $2°$ tilt grain boundary were fabricated by using diffusion bonding. The resulting boundary dislocations were observed by TEM and STEM, and electrical properties along the dislocations were measured by the DC method. It was found from the observations that the $(11\bar{2}0)/[1\bar{1}00]$ tilt grain boundary consists of $1/3[11\bar{2}0]$ dislocations which dissociate into two partial dislocations with the narrow separation distance of $2–3\,nm$. Meanwhile, in the case of the

(0001)/[11$\bar{2}$0] tilt grain boundary, two kinds of dislocations were primarily observed along the [11$\bar{2}$0] view. From the geometrical consideration, we concluded that the (0001)/[11$\bar{2}$0] tilt grain boundaries mainly consist of the three types of equivalent dislocations with $\boldsymbol{b} = 1/3[\bar{1}101]$, $1/3[0\bar{1}11]$, and $1/3[10\bar{1}1]$. Namely, one of the observed dislocations has the Burgers vector of $\boldsymbol{b} = 1/3[\bar{1}101]$ and the other one has the Burgers vector of $1/3[0\bar{1}11]$ or $1/3[10\bar{1}1]$. In addition, all of the three types of dislocations dissociate into two partial dislocations with the separation distance of 2–3 nm. It is interesting that the configurations of the partial dislocations are deviated from the boundary plane. This is because the edge components of the partials are not normal to the boundary plane. Note that the characteristic dislocation structures with the large Burgers vector of $1/3[1\bar{1}02]$ were formed only at the (0001)/[11$\bar{2}$0] 2° tilt grain boundary with a higher tilt angle. This dislocation structure also contained the $LiNb_3O_8$ phase around the core due to Li deficiency. It is believed that the narrower interval of geometrically formed dislocations should induce such characteristic structures. The electrical conduction measurement revealed that the (0001)/[11$\bar{2}$0] 2° tilt grain boundary exhibits high electrical conductivity after the reducing treatment, and the activation energy for electrical conduction is lower than that of the bulk region. It is suggested that the characteristic dislocation structure with the large Burgers vector brings about the distinct electrical conductivity.

ACKNOWLEDGMENTS

APPENDIX: ELECTRICAL CONDUCTIVITY OF REDUCED LINB$_3$O$_8$

$LiNb_3O_8$ is known to be a material with a wide band gap of 3.89 eV,[42] which was measured by the optical absorption method. However, electrical conductivity of the reduced $LiNb_3O_8$ had not been reported. Therefore, in order to investigate the effect of the $LiNb_3O_8$ phase on the electrical property of the (0001)/[11$\bar{2}$0] 2° tilt grain boundary, we fabricated single-phase $LiNb_3O_8$ samples and measured the electrical conductivity. $LiNb_3O_8$ samples were synthesized by the conventional mixed solid oxide method. As the starting materials, high purity (99.99%) oxide powders of Li_2CO_3 and Nb_2O_5 were used. The powders were milled with ZrO_2 balls at 70 rpm for 24 h in ethanol and dried at 100 °C. The mixed powders were calcined at 750 °C for 3 h in air. The calcined powders were pressed by uniaxial load into pellets of 15 mm diameter under 400 kg/cm^2 pressure. The pellets were finally sintered at 1100 °C for 2 h in air. The crystalline phases of the samples were analyzed by X-ray powder diffraction (XRD). Figure 13(a) shows the XRD pattern obtained in this study, which is
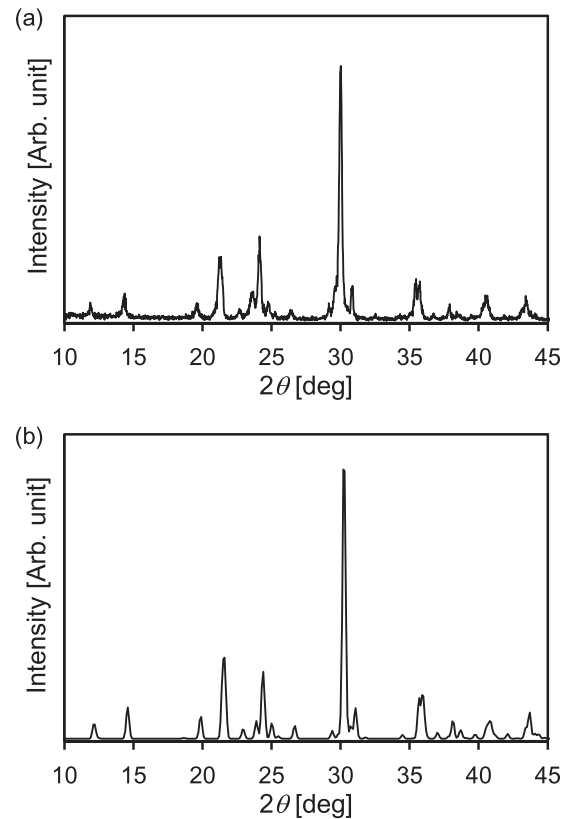

FIG. 13. (a) XRD pattern of the $LiNb_3O_8$ sample fabricated in this study. (b) Reported pattern of $LiNb_3O_8$ (PDF No. 01-075-2154).

consistent with a reported pattern of $LiNb_3O_8$ (Fig. 13(b)).[43] This means that the single phase of the $LiNb_3O_8$ compound was formed successfully. The density of the sintered pellets was estimated to be 4.0 g/cm^3. Some of the fabricated $LiNb_3O_8$ pellets were annealed at 500 °C for 10 h in a reducing atmosphere of Ar-4%H_2. Then, tungsten electrodes were sputtered on opposing faces of the pellets, and electrical conductivities were measured by applying dc voltage. Figure 14 shows the electrical conductivity of the $LiNb_3O_8$ samples with and without reduction treatment. It was found that the conductivity of $LiNb_3O_8$ is considerably increased by the reducing treatment. However, the conductivity is much lower than the
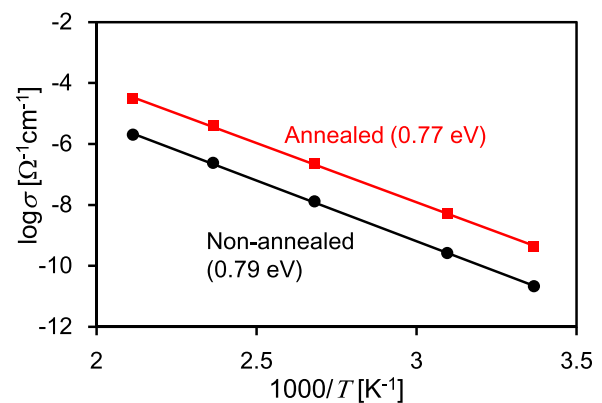

FIG. 14. Electrical conductivities of the $LiNb_3O_8$ samples in the temperature range of 20–200 °C. The red and black graphs show the conductivities of the samples with and without the reduction treatment, respectively. The numbers in the parentheses represent the activation energies.

estimated local conductivity at the $(0001)/[11\bar{2}0]$ 2° tilt boundary shown in Fig. 12. Additionally, the activation energy is inconsistent with that observed at the boundary (0.55 eV).

[1] N. Shibata, M. F. Chisholm, A. Nakamura, S. J. Pennycook, T. Yamamoto, and Y. Ikuhara, Science **316**, 82 (2007).

[2] D. L. Medlin, K. J. Erickson, S. J. Limmer, W. G. Yelton, and M. P. Siegal, J. Mater. Sci. **49**, 3970 (2014).

[3] C. L. Jia, A. Thust, and K. Urban, Phys. Rev. Lett. **95**, 225506 (2005).

[4] J. P. Buban, M. F. Chi, D. J. Masiel, J. P. Bradley, B. Jiang, H. Stahlberg, and N. D. Browning, J. Mater. Res. **24**, 2191 (2009).

[5] K. Takehara, Y. Sato, T. Tohei, N. Shibata, and Y. Ikuhara, J. Mater. Sci. **49**, 3962 (2014).

[6] A. H. Heuer, C. L. Jia, and K. P. D. Lagerlof, Science **330**, 1227 (2010).

[7] C. Elbaum, Phys. Rev. Lett. **32**, 376 (1974).

[8] D. Dimos, P. Chaudhari, and J. Mannhart, Phys. Rev. B **41**, 4038 (1990).

[9] R. De Souza, J. Fleig, J. Maier, Z. L. Zhang, W. Sigle, and M. Ruhle, J. Appl. Phys. **97**, 053502 (2005).

[10] S. Y. Choi, S. D. Kim, M. Choi, H. S. Lee, J. Ryu, N. Shibata, T. Mizoguchi, E. Tochigi, T. Yamamoto, S. J. L. Kang, and Y. Ikuhara, Nano Lett. **15**, 4129 (2015).

[11] I. Yonenaga, Y. Ohno, T. Yao, and K. Edagawa, J. Cryst. Growth **403**, 72 (2014).

[12] I. Sugiyama, N. Shibata, Z. C. Wang, S. Kobayashi, T. Yamamoto, and Y. Ikuhara, Nat. Nanotechnol. **8**, 266 (2013).

[13] A. Nakamura, K. Matsunaga, J. Tohma, T. Yamamoto, and Y. Ikuhara, Nat. Mater. **2**, 453 (2003).

[14] Y. Tokumoto, S. Amma, N. Shibata, T. Mizoguchi, K. Edagawa, T. Yamamoto, and Y. Ikuhara, J. Appl. Phys. **106**, 124307 (2009).

[15] Y. Ikuhara, Prog. Mater. Sci. **54**, 770 (2009).

[16] A. Nakamura, T. Mizoguchi, K. Matsunaga, T. Yamamoto, N. Shibata, and Y. Ikuhara, ACS Nano **7**, 6297 (2013).

[17] V. Metlenko, A. Ramadan, F. Gunkel, H. Du, H. Schraknepper, S. Hoffmann-Eifert, R. Dittmann, R. Waser, and R. De Souza, Nanoscale **6**, 12864 (2014).

[18] Y. Ikuhara, H. Nishimura, A. Nakamura, K. Matsunaga, T. Yamamoto, and K. P. D. Lagerlof, J. Am. Ceram. Soc. **86**, 595 (2003).

[19] A. Nakamura, K. Matsunaga, T. Yamamoto, and Y. Ikuhara, Philos. Mag. **86**, 4657 (2006).

[20] E. Tochigi, N. Shibata, A. Nakamura, T. Yamamoto, and Y. Ikuhara, Acta Mater. **56**, 2015 (2008).

[21] A. Nakamura, E. Tochigi, N. Shibata, T. Yamamoto, and Y. Ikuhara, Mater. Trans. **50**, 1008 (2009).

[22] E. Tochigi, N. Shibata, A. Nakamura, T. Mizoguchi, T. Yamamoto, and Y. Ikuhara, Acta Mater. **58**, 208 (2010).

[23] E. Tochigi, N. Shibata, A. Nakamura, T. Yamamoto, and Y. Ikuhara, J. Mater. Sci. **46**, 4428 (2011).

[24] E. Tochigi, A. Nakamura, T. Mizoguchi, N. Shibata, and Y. Ikuhara, Acta Mater. **91**, 152 (2015).

[25] A. Nakamura, E. Tochigi, J. Nakamura, I. Kishida, and Y. Yokogawa, J. Mater. Sci. **47**, 5086 (2012).

[26] F. C. Frank, Philos. Mag. **42**, 809 (1951).

[27] S. C. Abrahams, J. M. Reddy, and J. L. Bernstein, J. Phys. Chem. Solids **27**, 997 (1966).

[28] R. S. Weis and T. K. Gaylord, Appl. Phys. A **37**, 191 (1985).

[29] P. Nagels, "Experimental Hall effect data for a small-polaron semiconductor," in *The Hall Effect and Its Applications*, edited by C. L. Chien and C. R. Westlake (Plenum Press, New York, 1980), pp. 253–280.

[30] A. Dhar, N. Singh, R. K. Singh, and R. Singh, J. Phys. Chem. Solids **74**, 146 (2013).

[31] A. A. Ballman, J. Am. Ceram. Soc. **48**, 112 (1965).

[32] J. R. Carruthers, G. E. Peterson, M. Grasso, and P. M. Bridenbaugh, J. Appl. Phys. **42**, 1846 (1971).

[33] T. Volk and M. Wohlecke, *Lithium Niobate: Defects, Photorefraction and Ferroelectric Switching* (Springer-Verlag, Berlin, Heidelberg, 2008).

[34] Y. Ohno, T. Taishi, N. Bamba, and I. Yonenaga, J. Cryst. Growth **393**, 171 (2014).

[35] M. Peach and J. S. Koehler, Phys. Rev. **80**, 436 (1950).

[36] K. Ishizuka and N. Uyeda, Acta Crystallogr., Sect. A **33**, 740 (1977).

[37] M. A. Mccoy, S. A. Dregia, and W. E. Lee, J. Mater. Res. **9**, 2029 (1994).

[38] H. Akazawa and M. Shimada, J. Mater. Res. **22**, 1726 (2007).

[39] R. W. Balluffi, Phys. Status Solidi **42**, 11 (1970).

[40] T. E. Volin, K. H. Lie, and R. W. Balluffi, Acta Metall. **19**, 263 (1971).

[41] K. Otsuka, A. Kuwabara, A. Nakamura, T. Yamamoto, K. Matsunaga, and Y. Ikuhara, Appl. Phys. Lett. **82**, 877 (2003).

[42] P. P. Sahoo and P. A. Maggard, Inorg. Chem. **52**, 4443 (2013).

[43] M. Lundberd, Acta Chem. Scand. **25**, 3337 (1971).